Geochronology, 5, 391–403, 2023
https://doi.org/10.5194/gchron-5-391-2023
© Author(s) 2023. This work is distributed under
the Creative Commons Attribution 4.0 License.

Volcanism straddling the Miocene–Pliocene boundary on Patmos and Chiliomodi islands (southeastern Aegean Sea): insights from new ^{40}Ar / ^{39}Ar ages

Katharina M. Boehm[1], Klaudia F. Kuiper[1], Bora Uzel[2], Pieter Z. Vroon[1], and Jan R. Wijbrans[1]

[1]Department of Earth Sciences, Vrije Universiteit Amsterdam, 1081HV Amsterdam, the Netherlands
[2]Department of Geological Engineering, Dokuz Eylül University, 35160 İzmir, Turkey

Correspondence: Klaudia F. Kuiper (k.f.kuiper@vu.nl)

Received: 27 April 2023 – Discussion started: 2 May 2023
Revised: 18 August 2023 – Accepted: 29 August 2023 – Published: 11 October 2023

Abstract. The island of Patmos, in the eastern Aegean Sea, consists almost entirely of late Miocene to Pliocene volcanic rocks. The magmatism in the Aegean is governed by subduction of the African plate below the Eurasian plate, back-arc extension, slab rollback, slab edge processes and westward extrusion of central Anatolia to the west along the Northern Anatolian Fault into the Aegean domain. The evolution of the Aegean basin is that of a back-arc setting, with a southerly trend in the locus of both convergent tectonics and back-arc stretching, allowing intermittent upwelling of arc, lithospheric and asthenospheric magmas.

Here, we present new $^{40}Ar/^{39}Ar$ age data for Patmos and the nearby small island of Chiliomodi to place this volcanism in a new high-resolution geochronological framework. High-resolution geochronology provides a key to understanding the mechanisms of both the tectonic and magmatic processes that cause the extrusion of magma locally and sheds light on the tectonic evolution of the larger region of the back-arc basin as a whole.

The volcanic series on Patmos is alkalic, consistent with a back-arc extensional setting, and ranges from trachybasalt to phonolites, trachytes and rhyolites, with SiO_2 ranging from 51.6 wt % to 80.5 wt %, K_2O ranging from 2 wt % to 11.8 wt % and extrusion ages ranging from 6.59 ± 0.04 (0.14) Ma to 5.17 ± 0.02 (0.11) Ma. Volcanism on Patmos and adjacent Chiliomodi can be understood as a combination of mantle and crustal tectonic processes including the influence of transform faults and rotational crustal forces that also caused the widening of the southern Aegean basin due to two opposite rotational poles in the east and west and rollback of the subducting slab south of Crete.

1 Introduction

In the Aegean and western Anatolia regions Cenozoic magmatism is widespread and compositionally diverse. The evolution of the numerous volcanic centres is governed by (1) subduction-related, (2) back-arc and (3) intra-plate magmatic processes.

1. The subduction zone magmatism was governed by the composition of the subducting plate (Variscan continental basement rocks, intrusives, continental and oceanic crust, and sediment covers; e.g. Jacobshagen et al., 1978; Jacobshagen, 1994), the slab-derived fluids and the depth of magma generation, including assimilation and fractionation plus magma mixing.

2. Rollback of the subducting slab caused a gradual shift in the trench and trench-related processes to the south, forming the Aegean as an extensional, back-arc basin (McKenzie, 1978; Le Pichon and Angelier, 1981; Horvath and Berckhemer, 1982). Typically in a back-arc basin the overall stress field is extensional, allowing upwelling of magmas originating from deep sources. At the same time in back-arc settings, the relics of products of earlier compressional processes survive at depth, adding to diversification and mingling of the magmatic signatures of volcanic products. In addition to back-arc

extension, the Neogene tectonics of the (south)eastern Aegean region are dominated by the westward escape of Anatolia along the North Anatolian Fault Zone (NAFZ).

3. In addition to asthenospheric mantle upwelling facilitated by slab rollback, upwelling around the Hellenic slab edge is also a likely scenario in the eastern Aegean. The presence of an approximately vertical gap between the neighbouring Hellenic and Cyprus slabs is seen in tomographic and seismic data. The anomaly of the gap underlies western Anatolia at depth (e.g. Biryol et al., 2011) and reaches into the eastern Aegean in shallower levels (< 25 km, Govers and Fichtner, 2016).

Because of these indications of geometry the gap possibly also provides a channel for deeper asthenospheric magma sources in the eastern Aegean. In addition to the gap between the two slabs, there is speculation about the tearing of the Hellenic slab, which has been called upon for the interpretation of geochemical signals of volcanics in the eastern Aegean (Ersoy and Palmer, 2013; Palmer et al., 2019; Uzel et al., 2020). Understanding such volcanism adds to improved insights into the tectonic processes that underlie the formation of the Aegean back-arc basin, one of the best-studied back-arc basins globally (Jolivet and Brun, 2010; Van Hinsbergen and Schmid, 2012; Ring et al., 2017).

Regional setting

The island of Patmos ($\sim 34\,km^2$ in surface area) is one of several volcanic centres in the Aegean. Patmos is part of the Dodecanese island group, at present situated 100 km NW of Nisyros, which represents the present-day locus of arc volcanism in the eastern Aegean Sea (Fig. 1a). Patmos was located on thinned continental and back-arc crust and lithosphere by the end of the Miocene. Patmos is located centrally between two large metamorphic core complex provinces in the region, the Cyclades and the Menderes, which have both experienced extreme crustal thinning by low-angle normal faulting since the Miocene (Bozkurt and Mittwede, 2005; Van Hinsbergen and Schmid, 2012; Roche et al., 2018).

Late Miocene to Pliocene volcanism on Patmos is possibly largely influenced by the following major tectonic developments.

After the extension-driven first exhumation stage of the Cyclades dominated by low-angle normal faults, from the middle Miocene to the Pliocene the second stage of exhumation (e.g. Naxos core complex) followed with steep normal faults and horst–graben tectonics and triggered the opening of the southern Aegean basin (Wijbrans and McDougall, 1988; Lips et al., 2001). This late Miocene to Pliocene widening and thinning of the southern Aegean crust forced Crete further to the south and caused rotation with Euler poles just east of the Peloponnese in the west and just south of Patmos off the Anatolian coastline in the east (Kissel and Laj, 1988; Duermeijer et al., 1998). In addition to these rotations, transfer faulting also accommodated the $\sim$N–S extension during the widening of the southern Aegean (e.g. Jolivet et al., 2021; Gessner et al., 2013; Uzel et al., 2015). In the late Miocene to Pliocene, Patmos was situated in a tectonic transition zone, where transfer faulting also compensated for the transition between the Aegean and western Anatolian volcanic provinces. Further, Patmos has tectonic features associated with extensional graben structures related to the above-described core complex exhumation (e.g. Lykousis et al., 1995; Agostini et al., 2010; Ring et al., 2017). Tectonics accommodating the (eastern) rotational forces, the transition between Aegean and western Anatolian tectonics, and the extension following core complex exhumation may have governed the ascent of magma on Patmos and Chiliomodi at the Miocene–Pliocene boundary.

According to Roche et al. (2019), the marble basement of Patmos likely belongs to the Lower Cycladic Blueschist Nappe (LCBN). To the north, the LCBN is overthrust (Trans Cycladic Thrust) by the Upper Cycladic Blueschist Nappe (UCBN).

In the Dodecanese, tectonics features of the islands north and south of Patmos (e.g. Leros by Roche et al., 2018, or Samos by Ring et al., 1999) indicate ductile deformation, nappe emplacement and extension-related brittle E–W-striking normal faulting (Armijo et al., 1999, 2002). Tectonic studies on Patmos are limited. Wyers (1987a) only mentions a NW–SE-trending horst–graben structure and block faulting. Since horizons for correlating volcanic eruptions on Patmos are absent, it is difficult to come to a division of units on formal stratigraphical grounds. Without information on unconformities and deformation, only limited tectonic reconstructions are possible. However, with these limitations in mind, we will attempt to sketch the tectonic evolution of Patmos in the light of our newly obtained ages while taking into account information from regional stress fields as deduced from neighbouring islands and areas.

Volcanism on Patmos was active during the Messinian (late Miocene) and the early Zanclean (Pliocene), a period of anomalously low water tables throughout the Mediterranean domain that cause decompression in the already thinned crust underlying Patmos island. The island of Patmos is almost entirely volcanic and offers a range of potassium-rich rock types, including trachyandesites, trachytes, phonolites and rhyolites (Robert, 1973; Fig. 1b). The oldest volcanic rocks on Patmos are phonolites, with other volcanic rocks being roughly 1 Ma younger (Wyers, 1987a).

Phonolites derive from silica-undersaturated mafic magmas and are commonly found in intra-plate settings, intracontinental rifts and oceanic island settings. The phonolites of Patmos are a rare example of phonolite occurrence in or near a volcanic arc or back-arc setting. In western Anatolia, west of the current slab gap as indicated by tomography (e.g. Biryol et al., 2011; Fig. 1a), the volcanic centre of Foca is one of the few nearby localities where phonolites are de-

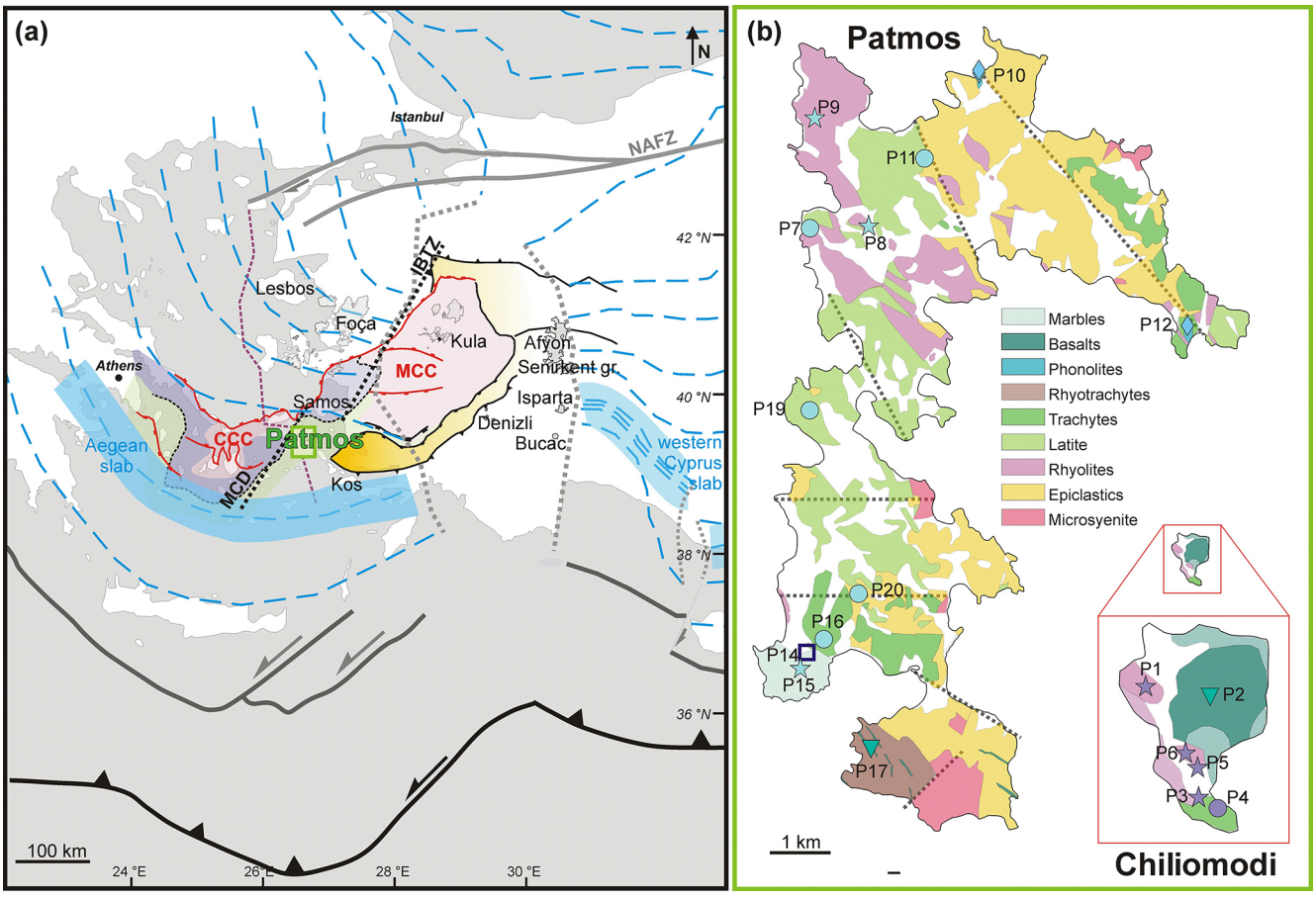

Figure 1. **(a)** Map of the Aegean and Anatolian region modified from Biryol et al. (2011), Ersoy and Palmer (2013), Uzel et al. (2015), Govers and Fichter (2016), and Roche et al. (2019). Recent positions of the northward-dipping slabs are indicated by dashed blue isolines (50 km distance). The blue band indicates the position of the South Aegean Active Volcanic Arc at about 100 km slab depth (same depth is marked on the western Cyprus slab). Between the Aegean slab and the western Cyprus slab, a gap, with complex vertical geometry (dashed purple and grey lines), has been observed in tomographic and seismic data (Biryol et al., 2011; Govers and Fichter, 2016). Volcanic fields in western Anatolia (grey areas) are compared to Patmos volcanics in this paper. Patmos is highlighted with a green rectangle. CCC stands for Cycladic Core Complex, MCC stands for Menderes Core Complex and NAFZ stands for North Anatolian fault zone. **(b)** Simplified geologic map of Patmos modified from Galeos (1993). Our sampling sites are indicated with symbols: stars are rhyolite, downward-facing triangles are trachybasalt, circles are trachyte, diamonds are phonolites and the square is marble. Faults are indicated as dashed grey lines.

scribed (Akay and Erdoğan, 2004; Altunkaynak et al., 2010). Altunkaynak et al. (2010) performed laser step heating of bulk plagioclase of a phonolite (SF-11) and reports an age of 14.12 Ma, significantly older than the ones on Patmos. Besides the phonolites of Foca, in proximity of Isparta, below the tomographically indicated slab gap, two occurrences of phonolites are described in the literature. In the area of Afyon (Akal et al., 2013; Prelević et al., 2015) and the Senirkent graben (Elitok, 2019) phonolites were studied, but no absolute high-precision time constraints have been published so far. In summary, although a minor component, several occurrences of Miocene phonolites are described in the eastern Aegean and western Anatolian volcanic province.

In this paper we provide new high-resolution $^{40}Ar/^{39}Ar$ ages for the different volcanic units on Patmos and the small neighbouring island of Chiliomodi. These new data allow us to complement and refine existing datasets from Wyers (1987a) and place these results in a tectonic context where we will assess the possible roles of (a) slab rollback and contemporaneous back-arc extension (e.g. Palmer et al., 2019; Pe-Piper and Piper, 2007), (b) possible periodic upwelling of sub-continental lithospheric or asthenospheric melts through gap(s) in the subducting slab, and (c) tectonic regime changes in the area at the time. The exhumation of core complexes and the westward propagation of the Northern Anatolian Fault (NAF) into the Aegean around 5 Ma resulted in changes in extensional tectonics and fault patterns (Armijo et al., 1999, 2002). Here we want to constrain the potential links between changing tectonic stress fields and volcanism on Patmos.

2 Methodology

Samples were collected from different units on both Patmos and Chiliomodi based on the geological map of Patmos (Galeos, 1993), the thesis of Wyers (1987a), and the publications Wyers and Barton (1986) and Wyers (1987b) (see coordinates in Table 1). All sample preparations and analyses of this study were performed at Vrije Universiteit Amsterdam, the Netherlands. Unaltered, cleaned samples were crushed and subsequently split into fractions for mineral separation for $^{40}Ar/^{39}Ar$ geochronology and for powdering for major elements. We analysed each sample for major elements and measured $^{40}Ar/^{39}Ar$ ages on sanidine and/or biotite phenocrysts.

2.1 Major elements

Major element concentrations were measured by X-ray fluorescence spectroscopy (XRF) on fused glass beads on a Panalytical AxiosMax instrument. Sample powders were ignited at 1000 °C for 2 h to determine the loss on ignition (LOI) before being mixed with Li_2B_4O7 / $LiBO_2$ (1 : 4 dilution) and fused to glass beads at 1150 °C. All XRF results are reported on a volatile-free basis and normalized to 100 wt %, and Fe is expressed as total ferrous iron (FeO*). Precision and accuracy for major elements were both better than 2 % relative standard deviation (RSD).

2.2 $^{40}Ar/^{39}Ar$ geochronology

Sanidine and/or biotite separates were obtained using standard heavy mineral separation procedures (Frantz magnet, heavy liquid separation). A tabletop Jeol SEM was used to assess potassium contents of the minerals. Samples were hand-picked under an optical microscope, leached with diluted HNO_3 and cleaned with deionized water in an ultrasonic bath. Samples and standards (Fish Canyon sanidine) were wrapped in Al foil, loaded in Al cups and irradiated for 12 h in the CLICIT facility of the OSU TRIGA reactor at Oregon State University (VU114). After irradiation, multiple grains samples and standards were loaded into a copper disc with holes of 2 mm diameter, pre-heated under vacuum for > 24 h at 250 °C and heated overnight at 120° in an ultra-high vacuum extraction line. The mineral grains were fused at 12 % beam intensity of a focused 50 W continuous wave Synrad 48-5 series CO_2 laser system. The released gas was cleaned using hot getters (SAES NP10, ST172, Ti sponge) and a Lauda cold trap at −70 °C to eliminate reactive gases. The purified Ar was analysed isotopically on a Thermo Fisher Helix MC multi-collector noble gas mass spectrometer, with two Faraday collectors with 10^{13} Ohm resistor amplifiers (^{40}Ar and ^{39}Ar beams) and three pulse-counting compact discrete diode (CDD) multiplier collectors (^{38}Ar, ^{37}Ar and ^{36}Ar beams). The H2, H1, AX and L1 detectors (m/e: 40, 39, 38 and 37, respectively) are fitted with standard slits resulting in a resolution of ca. 850 to resolve hydrocarbon interferences from the argon isotope signals, and the L2 channel (m/e: 36) was fitted with a high-resolution slit (resolution > 1500 to resolve $^{12}C_3$ and $^{1}H^{35}Cl$ from ^{36}Ar). Gain calibration for the Faraday and CDD cups was done by peak jumping of an air ^{40}Ar beam (∼ 50 fA) on all detectors in static mode. Intensities are regressed to time zero, and gain calibration factors are determined relative to the AX-CDD. Between the sample measurements system blanks were measured regularly every three steps, and air pipette aliquots of $^{40}Ar/^{36}Ar$ were analysed for monitoring the mass discrimination. The software ArArCALC2.5 (Koppers, 2002) and the air ratio of 298.56 ± 0.31 of Lee et al. (2006) were used. Interfering isotope production ratios can be found in Table S1 in the Supplement. The reported full external error includes analytical uncertainty and includes error in J values, standard age and decay constants with 2σ uncertainty.

3 Results

3.1 Petrography

The trachybasalt (P2) sampled on Chiliomodi contains pristine olivine (ol), clinopyroxene (cpx), plagioclase (plag) and oxides. It also contains gabbroitic microcumulates of plag, ol and cpx. The sample has a coarse matrix and does not show any signs of alteration (no sericite in plag, no iddingsite in ol).

The basaltic trachyandesite (P17) contains about 35 % plag, 30 % K-feldspar, 20 % sodalite, 10 % nepheline and 5 % leucite. It has a coarse plag-rich groundmass (grm) and a porphyritic texture.

The most common phenocrysts observed in the trachytes of Patmos and Chiliomodi are K-feldspar (kfsp), pyroxene (px), biotite (bt) and plagioclase (plag) in a porphyritic groundmass. Some trachytes have big kfsp phenocrysts (e.g. P4, P7). The trachyte (P11) has a fine qtz–bt matrix with phenocrysts of plag (∼ 40 %), quartz (qtz) (∼ 30 %), bt (∼ 20 %) and kfsp (∼ 10 %). Trachyte P13 has similar mineralogy but shows subhedral plag crystals. The trachyte P7 does not show signs of alteration and contains ∼ 30 % quartz (qtz) and ∼ 20 % kfsp as well as cpx, bt and ol. The porphyric texture is dominated by big phenocrysts of kfsp and cpx and ∼ 35 % grm. It also contains cumulates of ol, px and fsp. Olivine (15 %) is also observed in the trachyte P16.

The rhyolites have relatively few crystals of mostly kfsp and cpx phenocrysts. Rhyolite P1 also contains plag and bt, in rhyolite P3 zeolites are also observed, rhyolite P5 is very altered and contains mainly clay minerals, and rhyolite P6 is also slightly altered. P8 is a glassy rhyolite that also contains titanite and an altered groundmass (clay minerals). The rhyolite P9 is a relatively fresh rock; is very fine grained; and contains ∼ 49 %glass, ∼ 35 % kfsp, 15 % bt, and ∼ 1 % cpx.

The phonolites sampled on Patmos contain phenocrysts and clusters of kfsp (∼ 25 %–39 %), sodalite (∼ 15 %–35 %),

Table 1. WGS84 coordinates of sample locations on Chiliomodi and Patmos.

Sample no.	Outcrop no.	Coordinates latitude (WGS84)	Coordinates longitude (WGS84)	Description of locality	Rock type
G16P01A	G16_P01	37.30805	26.60189	Chiliomodi, behind the church	Andesitic inclusions in rhyolite
G16P01B	G16_P01	37.30805	26.60189	Chiliomodi, behind the church	Glassy rhyolite, partly red oxidized
G16P02	G16_P02	37.30757	26.60439	Chiliomodi, hill top	Trachybasalt, weathered platy
G16P03	G16_P03	37.30433	26.60421	Chiliomodi	Rhyolite
G16P04	G16_P04	37.30407	26.60456	Chiliomodi, same outcrop as P03	Trachyte
G16P05	G16_P05	37.30538	26.60384	Chiliomodi	Rhyolite, soft (clay)
G16P06	G16_P06	37.30589	26.60330	Chiliomodi	Rhyolite
G16P07	G16_P07	37.35252	26.53565	N of Skala, quarry, after military left	Trachyte, very fresh
G16P08	G16_P08	37.35146	26.53671	Next to quarry of P07	Rhyolite
G16P09	G16_P09	37.36709	26.53660	NW end of Patmos	Rhyolite
G16P10A	G16_P10	37.37302	26.56528	N (middle peninsula)	Phonolite
G16P10B	G16_P10	37.37302	26.56528	N (middle peninsula)	Phonolite
G16P11	G16_P11	37.36069	26.55787	N of Kampos	Trachyte
G16P12	G16_P12	37.33780	26.60338	NE peninsula, south side, ship beach	Phonolite
G16P13	G16_P13	37.35140	26.54642	W of Kampos	Trachyte
G16P14	G16_P14	37.29298	26.53527	Marble quarry	Marble from quarry owner
G16P15	G16_P15	37.29093	26.53447	Marble quarry	Rhyolite dyke in marble
G16P16	G16_P16	37.29442	26.53782	Marble quarry	Trachyte
G16P17	G16_P17	37.28169	26.54934	Southernmost Patmos	Basaltic trachyandesite dyke in rhyodacitic series
G16P18	G16_P18	37.28012	26.54773	Southernmost Patmos	Feldspar
G16P19	G16_P19	37.32637	26.53605	NW of Skala	Trachyte
G16P20	G16_P20	37.30053	26.54509	S Patmos	(Granitic?) dyke

chlorite (∼ 20 %–30 %), amphibole (8 %–10 %), biotite (up to 15 % in P10B), nepheline (P12), orthopyroxene, clinopyroxene and titanite (P10A, P12). The matrix consists mainly of plag and chlorite and is much finer and contains more glass in P10B than P10A. Thin-section photos can be found in the Supplement (Fig. S1).

3.2 Major element chemistry

Results of major-element XRF analyses are listed in Table 3. The SiO_2 content in the selected volcanic rock samples ranges from 51.6 wt % to 80.5 wt %. The total alkali content ($K_2O + Na_2O$) of the samples ranges from 6.4 wt % to 14.5 wt %, K_2O varies between 2 wt % and 11.8 wt %, and Na_2O varies between 1.4 wt % and 7.9 wt % (except P15 which has 0.11 wt % Na_2O). Accordingly, eight samples are classified as rhyolites (P1B, P3, P5 and P6 from Chiliomodi; P6, P8, P9 and P15 from Patmos), five as trachytes (P4 from Chiliomodi; P7, P13, P16, P19 and P11 from Patmos), three as phonolites (P10A, P10B and P12 from northern Patmos), one as andesite (P1A enclave in P1B), one as basaltic trachyandesite (P17 dyke in southern Patmos) and one as trachybasalt (P2 from Chiliomodi) (Fig. 2a; Le Bas et al., 1986). The K_2O/Na_2O ranges from 0.45 to 8.35 (P15 72.61). The trachytes P11, P16 and P19 and the rhyolites P8 and P9 have the lowest Na_2O content and thus the highest K_2O/Na_2O ratios, while the phonolites are the most sodic rocks on Patmos ($K_2O/Na_2O < 1$) (Fig. 2b).

3.3 Argon geochronology

The $^{40}Ar/^{39}Ar$ results indicate that active volcanism on Patmos occurred between ∼ 5.7 and 6.0 Ma with a first pulse of activity around 6.5 Ma (Fig. 3; Tables 2 and S1 in the Supplement). Nearby Chiliomodi island was active from ∼ 5.4 to 5.2 Ma. Rhyolite P1 yields a total fusion age of 5.17 ± 0.02 (0.11) Ma (analytical uncertainty + J error, with full external error in parentheses, 2σ). The radiogenic $^{40}Ar^*$ was on average 87 % (77 %–94 %) and the mean square weighted deviation (MSWD) was 0.46 ($n = 19/20$). Rhyolite P3 contains anorthoclase, with K contents ranging between ∼ 2.0 wt % and 2.6 wt % (based on pre-irradiation sample screening on tabletop SEM) with K/Ca ratios of ∼ 14–15 (based on the conversion of the measured $^{39}Ar_K/^{37}Ar_{Ca}$ ratio). Two size fractions yielded relatively low radiogenic $^{40}Ar^*$ yields of ∼ 35 %–49 %. The smaller size fraction of 355–500 µm had slightly lower radiogenic $^{40}Ar^*$ (∼ 35 %) and resulted in a total fusion age of $5.34 \pm (0.05\ (0.12)$ Ma, while the coarser fraction of 500–1000 µm resulted in 5.40 ± 0.03 (0.12) Ma (MSWD of 0.18 and 0.27, where $n = 18/19$ and $n = 18/20$, respectively). Two size fractions from rhyolite P4 yielded 5.39 ± 0.07 (0.13) Ma (355–500 µm) and $5.41 \pm (0.03)\ 0.12$ Ma (500–1000 µm). The radiogenic $^{40}Ar^*$

https://doi.org/10.5194/gchron-5-391-2023

Table 2. Summary of $^{40}Ar/^{39}Ar$ results. Includes sample characteristics, potassium content in minerals, total fusion age, fully external error, MSWD, number of measurements, radiogenic ^{40}Ar, ^{39}Ar, K/Ca ratio, inverse isochron intercept, inverse isochron age, and MDF and J values used.

Sample ID	G16P1	G16P3	G16P3 big	G16P4	G16P4 big	G16P6	G16P7	G16P7 bt	G16P9	G16P10 non-mag	G16P10 second	G16P11 non-mag	G16P11 second	G16P11 bt	G16P13 bt
Sample ID Ar	KB1	KB2	KB3	KB4	KB5	KB6	KB7	KB8	KB9	KB10	KB11	KB12	KB13	KB14	KB15
Mineral	sanidine	sanidine	sanidine	sanidine	sanidine	sanidine	sanidine	biotite	sanidine	sanidine	sanidine	sanidine	sanidine	biotite	biotite
Grain size (µm)	355–500	355–500	500–1000	355–500	500–1000	355–500	355–500	400–500	355–500	355–500	355–500	355–500	355–500	355–500	355–500
Additional notes	NA	NA	NA	NA	NA	NA	NA	Density 3.05–3.22	NA	Frantz max − 2	Frantz max 0–max − 2	Frantz max − 1.5	Frantz max 0–max − 1.5	NA	NA
K (wt %) (SEM)	3.7	2.0	2.6	3.2	4.4	3.9	6.7	3.0	4.0	2.2	2.2	4.5	4.5	5.8	4.9
no. of grains per fusion	5	10	8	6	5	5	3	7	5	9	9	4	4	3	4
Rock type	rhyolite	rhyolite	rhyolite	trachyte	trachyte	rhyolite	trachyte	trachyte	rhyolite	phonolite	phonolite	trachyte	trachyte	trachyte	trachyte
Locality	Chiliomodi	Chiliomodi P3 = P4	Chiliomodi P3 = P4	Chiliomodi P4, same outcrop as P3	Chiliomodi P4, same outcrop as P3	Chiliomodi	N of Skala, quarry	N of Skala, quarry	NW Patmos	N Patmos (middle)	N Patmos (middle)	N of Kampos	N of Kampos	N of Kampos	W of Kampos
Age (Ma)	5.17	5.34	5.40	5.39	5.41	5.33	5.63	5.84	5.98	6.54	6.59	5.69	5.84	4.23	5.87
±2σ analytical error + J error	0.02	0.05	0.03	0.07	0.03	0.03	0.03	0.05	0.05	0.06	0.04	0.03	0.03	0.13	0.05
±2σ full external error	0.11	0.12	0.12	0.13	0.12	0.11	0.12	0.13	0.13	0.15	0.14	0.12	0.12	0.16	0.13
MSWD	0.46	0.18	0.27	0.04	0.44	0.29	0.37	0.51	1.71	2.73	0.38	0.49	0.73	0.24	1.23
N (N total)	19 (20)	18 (19)	18 (20)	13 (15)	14 (20)	14 (15)	20 (20)	10 (15)	12 (15)	9 (14)	15 (19)	19 (20)	19 (20)	12 (20)	13 (15)
^{40}Ar (%)	88.6	33.5	50.1	32.4	61.2	64.1	80.3	71.3	73.8	64.2	98.7	80.7	87.8	12.7	60
K/Ca	29.1	14.2	15.3	10.8	11.4	12	26.8	8.2	19.6	13.2	13.8	19.1	18.5	54.1	11.6
$^{40}Ar/^{36}Ar$ inverse isochron intercept	298.5	295.8	300.5	299.2	300.9	302.6	303.2	310.4	298.3	291.2	305.1	297	301	293.7	294.1
±2σ analytical error + J error	6.6	5.4	2.4	4.2	3.8	5.1	6.3	16.4	6.4	20	7.8	5.1	7.1	14.7	11.5
Inverse isochron age	5.17	5.43	5.38	5.37	5.39	5.29	5.62	5.77	5.98	6.62	6.56	5.70	5.83	4.70	5.93
±2σ analytical error + J error	0.03	0.18	0.04	0.14	0.04	0.05	0.04	0.12	0.06	0.24	0.06	0.03	0.03	1.38	0.15
±2σ full external error	0.11	0.21	0.12	0.18	0.12	0.12	0.12	0.17	0.14	0.27	0.15	0.12	0.13	1.38	0.20
MSWD	0.48	0.13	0.11	0.040	0.35	0.11	0.27	0.30	1.90	2.92	0.17	0.5	0.75	0.22	1.29
MDF	1.01002	1.01002 and 1.004184	1.004762	1.004184	1.004762	1.004184	1.004184	1.009357	1.009357	1.004184	1.008591	1.004184	1.004762	1.009357	1.009357
1 SD (%)	0.18	0.18 and 0.27	0.20	0.27	0.20	0.27	0.27	0.13	0.10	0.27	0.37	0.27	0.20	0.13	0.13
J	0.0017599	0.0017599	0.0018654	0.0017599	0.0018654	0.0017676	0.0017676	0.0018529	0.0018457	0.0017676	0.0018658	0.0017676	0.0018654	0.0018529	0.0018457
1 SD (%)	0.20	0.20	0.20	0.20	0.20	0.20	0.20	0.33	0.33	0.20	0.20	0.20	0.20	0.33	0.33

NA: not available.

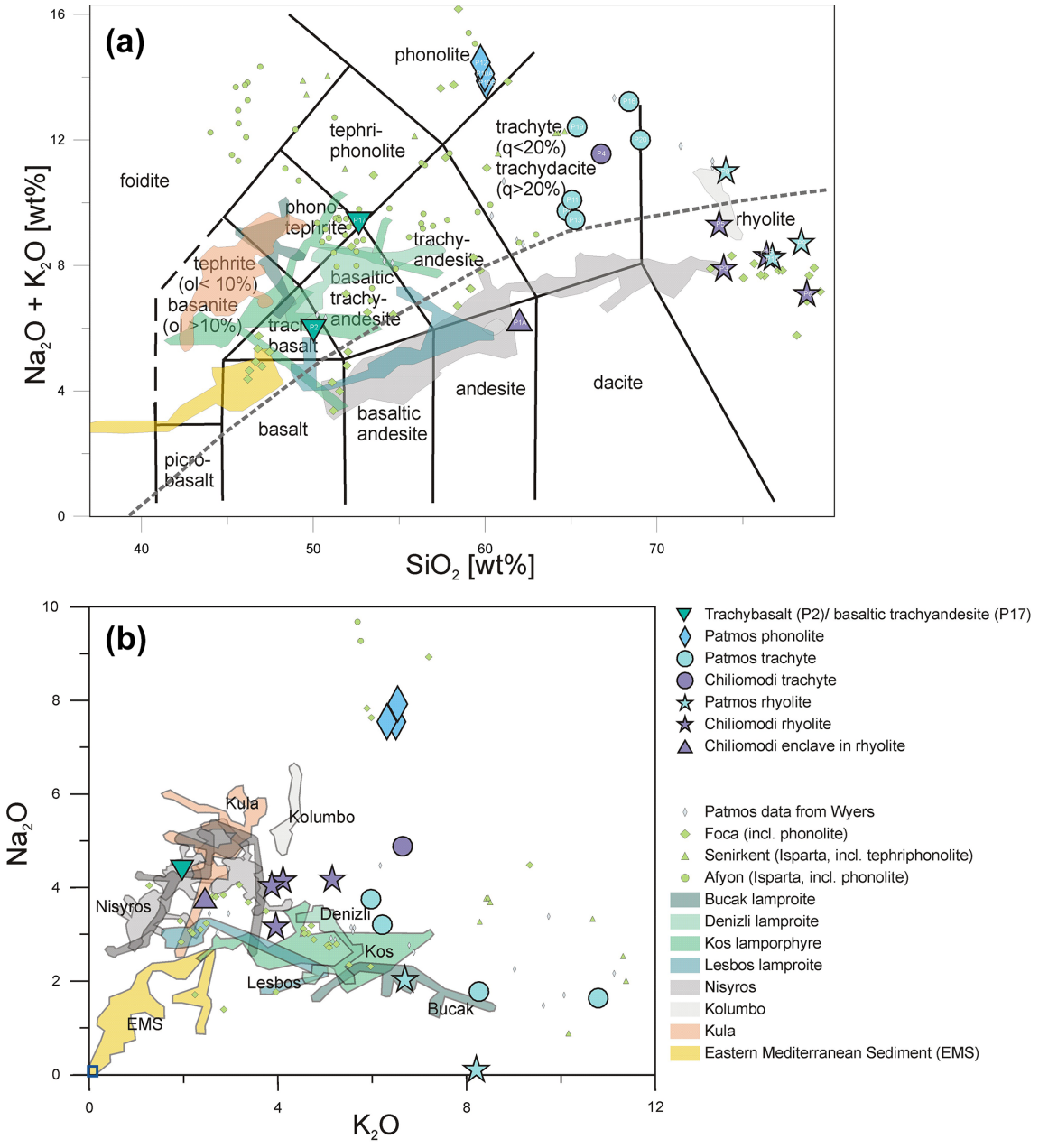

Figure 2. **(a)** Total alkali versus silica diagram (TAS, after Le Bas et al., 1986) for volcanic rocks of Patmos, the eastern Aegean and western Anatolia. The same symbols are used in both panels. Data for fields of western Anatolia are from Altunkaynak et al. (2010), Akay and Erdoğan (2004) (Foça); Elitok (2019) (Senirkent); Akal et al. (2013), Prelević et al. (2015) (Afyon); Çoban and Flower (2007) (Bucak); Prelević et al. (2012) (Denizli), Soder et al. (2016) (Kos); Pe-Piper et al. (2014) (Lesbos), Klaver et al. (2015, 2016) (Eastern Mediterranean Sediment, EMS; Alıcı et al. (2002) (Kula)). **(b)** Na_2O versus K_2O diagram. Note the large diversity in both high Na_2O and K_2O content of the Patmos volcanic rock compared to Aegean and western Anatolian volcanic rocks and EMS.

was on average 31 % and 59 %, respectively, for the finer and coarser fraction (MSWD of 0.04 and 0.44, where $n = 13/15$ and $14/20$, respectively). The rhyolite P6 yielded $5.33 \pm 0.03\,(0.11)$ Ma (^{40}Ar* ∼ 62 %, MSWD of 0.27, $n = 14/15$).

The rhyolite and trachytes of Patmos island yielded slightly older ages than the rhyolites from Chiliomodi. Rhyolite P9 resulted in $5.98 \pm 0.05\,(0.13)$ Ma (^{40}Ar* ∼ 72 %, MSWD of 1.71, $n = 12/15$). Trachyte P7 resulted in a sanidine age of $5.63 \pm 0.03\,(0.12)$ Ma (^{40}Ar* 80 %, MSWD of 0.37, $n = 20/20$) and a biotite age of $5.84 \pm 0.05\,(0.13)$ Ma (^{40}Ar* 71 %, MSWD of 0.51, $n = 10/15$). Three separates of trachyte P11 were measured. The diamagnetic sanidine fraction yielded $5.69 \pm 0.03\,(0.12)$ Ma, and the slightly more

Table 3. XRF major element data (LOI-corrected; in wt %).

Sample	SiO_2	TiO_2	Al_2O_3	FeO*	MnO	MgO	CaO	Na_2O	K_2O	TiO_2	P_2O_5	LOI
P01A	64.09	0.49	16.66	3.78	0.07	3.18	5.04	3.87	2.53	0.17	0.10	0.08
P01B	77.30	0.13	12.85	0.46	0.05	0.07	0.65	4.20	4.18	0.01	0.11	0.05
P02	51.56	1.74	18.01	8.16	0.16	4.90	8.33	4.49	2.03	0.53	0.09	0.11
P03	75.16	0.18	13.57	1.15	0.06	0.38	1.34	4.11	3.93	0.04	0.09	0.11
P04	67.77	0.39	16.63	2.02	0.05	0.25	1.05	4.96	6.75	0.10	0.02	0.07
P05	74.72	0.17	13.74	1.05	0.04	0.14	0.66	4.24	5.22	0.01	0.01	0.43
P06	80.49	0.14	10.52	0.81	0.04	0.12	0.57	3.25	4.03	0.02	0.01	0.11
P7	64.99	0.61	16.56	3.28	0.09	1.19	3.20	3.78	5.99	0.23	0.08	0.16
P8	74.17	0.20	13.20	1.14	0.05	0.09	0.09	1.48	9.55	0.01	0.01	0.13
P9	78.55	0.19	11.23	1.05	0.05	0.06	0.11	2.05	6.70	0.01	0.01	0.16
P10A	60.13	0.42	20.89	2.27	0.21	0.33	1.60	7.58	6.53	0.03	0.00	1.17
P10B	60.23	0.41	20.96	2.26	0.21	0.31	1.70	7.57	6.32	0.03	0.00	0.75
P11	65.34	0.70	17.66	3.86	0.05	1.54	0.56	1.80	8.31	0.07	0.11	0.30
P12	59.89	0.40	21.00	2.26	0.21	0.21	1.52	7.94	6.55	0.02	0.00	0.36
P13	65.53	0.71	17.07	3.76	0.04	0.73	2.27	3.23	6.25	0.25	0.15	0.10
P15	76.91	0.19	13.17	0.80	0.03	0.40	0.08	0.11	8.21	0.01	0.07	0.20
P16	68.49	0.29	16.37	1.53	0.03	0.03	0.02	1.41	11.80	0.02	0.00	0.10
P17	53.05	1.41	18.14	6.15	0.12	5.12	5.92	3.84	5.60	0.52	0.11	0.91
P19	65.62	0.68	16.11	3.19	0.04	0.69	0.79	1.63	10.83	0.28	0.13	0.15
P20	69.14	0.67	16.60	0.78	0.00	0.35	0.19	1.69	10.31	0.15	0.11	0.36

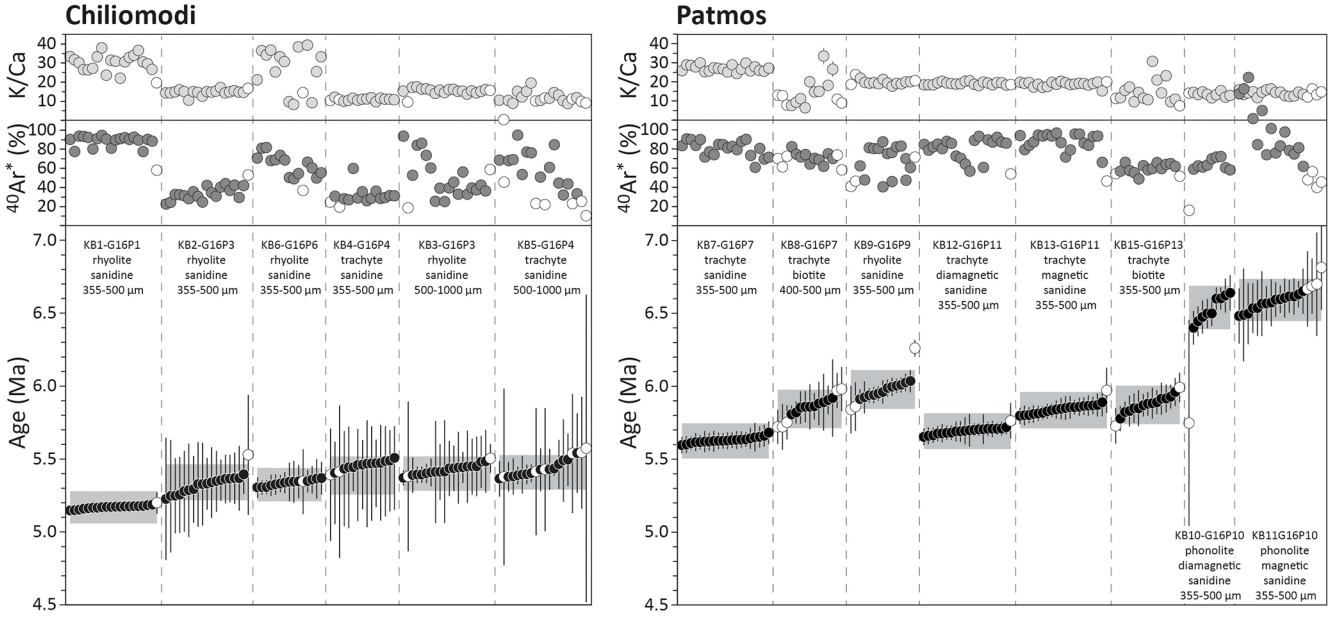

Figure 3. The $^{40}Ar/^{39}Ar$ diagram shows individual fusion ages with 2 SD analytical uncertainties for individual analyses and weighted mean ages.

magnetic sanidine yielded $5.84 \pm 0.03\,(0.12)$ Ma. The second sanidine fraction had a higher $^{40}Ar^*$ yield (88 % average) than the first sanidine fraction (80 % average). Based on visual inspection, the biotites appeared to have sufficient quality, but based on the $^{40}Ar/^{39}Ar$ ages we conclude the biotites were too altered and did not yield reliable ages. Their $^{40}Ar^*$ yield was only 13 %, indicating severe alteration, and therefore the biotite data are excluded. Trachyte P13 yielded a weighted mean age for biotite of $5.87 \pm 0.05\,(0.13)$ Ma ($^{40}Ar^*$ 60 %, MSWD of 1.23, $n = 13/15$), which due to its high $^{40}Ar^*$ content was considered to be the only analytically reliable biotite age result.

Phonolites are the oldest rocks of this study. Two fractions of 355–500 µm sanidine were dated from sample P10. The

first fraction contained the non-magnetic sanidines, while the second fraction contains slightly more magnetic sanidines of the same grain size range. The most non-magnetic and slightly magnetic fraction yielded total fusion ages of $6.54 \pm 0.06\,(0.15)$ Ma (^{40}Ar* 64 %, MSWD of 2.73, $n = 19$) and $6.59 \pm 0.04\,(0.14)$ Ma (^{40}Ar* 96 %, MSWD of 0.38, $n = 15$). Note that none of the samples in this study show evidence of excess argon.

4 Discussion

4.1 Reproducibility of ^{40}Ar/^{39}Ar ages

We analysed both sanidine and biotite of Patmos sample P7 yielding a biotite age that is 0.219 ± 0.056 Ma older than the sanidine. Coevally erupted sanidines and biotites indeed do not always match in age (e.g. Kuiper et al., 2004; Hora et al., 2010). Excess Ar in biotite could be a reason for this age difference but is unlikely for our samples as the ^{40}Ar/^{36}Ar inverse isochron intercepts of the analysed fusion experiments do not deviate from the atmospheric argon ratio. Alternatively, the older biotite ages can be explained by neutron irradiation excess ^{39}Ar recoil from K-depleted chlorite cleavage zones in partially altered biotites (Smith et al., 2008; Hess et al., 1987). Alteration causes the transition of K-bearing biotite laminae to K-free chlorite laminae, which are more open to recoil of ^{39}Ar and thus the leakage of ^{39}Ar from the crystal, with the apparent ^{40}Ar/^{39}Ar ratio increases leading to higher observed ^{40}Ar/^{39}Ar ages (the opposite of other alteration processes that often lower the total fusion ages). Typically such chloritization processes are accompanied by the uptake of substantial amounts of atmospheric argon. In addition, this can be explained by partial closure of biotite before the eruption, while sanidine remains open due to its lower closure temperature and can consequently degas efficiently for longer in the magma chamber (Hora et al., 2010). This process depends on whether (partial) isotopic equilibrium with the atmosphere was reached at modest pressure (shallow pre-eruption storage) and also depends on cooling rates at the time of the eruption. If the closure temperature of biotite is higher than the eruption temperature, excess ^{40}Ar can be locked in the biotite and in situ production of ^{40}Ar* starts, i.e. the clock starts before the eruption. Extraneous ^{40}Ar in biotite can thus lead to older ages than in sanidine, i.e. pre-eruption ages. The ability to analyse this difference between the biotite and sanidine system proves the low limit of analytical uncertainty in the measurements.

We also analysed multiple sanidine sample splits with either different grain sizes or different magnetic behaviour. We did not observe a relation between grain size and age. However, differences in magnetic properties seem to yield different ages, with the least magnetic (or diamagnetic) sanidine yielding younger ages with slightly lower ^{40}Ar* contents (Fig. 3). Pure sanidine is weakly diamagnetic, but small amounts of Fe cations or magnetic grains or inclusions can result in increased magnetic susceptibility (e.g. Biedermann et al., 2016). Paramagnetic impurity ions can be incorporated into the feldspar structure; e.g. Fe^{3+} can replace Al^{3+}. Magnetite may form by exsolution of Fe from the feldspar structure, usually described as a response to cooling from high temperatures (Biedermann et al., 2016; Hounslow and Morton, 2004, and references therein). Small amounts of submicroscopic ferromagnetic mineral inclusions, e.g. magnetite, are described for sanidine, often occurring along grain boundaries and cleavage domains (Finch and Klein, 1999). From this, we infer that the sanidine grains with slightly higher magnetic susceptibility are prone to contain submicroscopic ferromagnetic inclusions, and we hypothesize that these may potentially contain submicroscopic inclusions, which may either contain excess ^{40}Ar or play a role in hosting recoiled ^{39}Ar produced by neutron activation. Anderson et al. (2000) described magnetite inclusions in sanidine that might have equilibrated via melt channels that formed along cleavage planes. If such an equilibration occurred, minor amounts of ambient ^{40}Ar may have entered the crystal via melt channels.

In addition, we observed variation in radiogenic ^{40}Ar* within and between different grain sizes from the same sample. Sanidine of P3 from Chiliomodi island yielded 22 %–44 % (355–500 µm) and 25 %–93 % ^{40}Ar* (500–1000 µm). As this variation in radiogenic ^{40}Ar* is not linked to any age variation (Fig. 3), we find that the ages obtained from this sample are reproducible. The ^{40}Ar/^{36}Ar isochron intercepts of those samples overlap with ^{40}Ar/^{36}Ar atmospheric ratios, meaning that the variability in radiogenic ^{40}Ar* was unlikely caused by excess argon (e.g. from fluid inclusions). Therefore, we infer that inclusions containing atmospheric argon were present in these mineral fractions and that this higher contribution of atmospheric Ar resulted in lower ^{40}Ar* percentage.

In summary, while we note some significant spread in ages, the internal reproducibility within each sample fraction is excellent.

4.2 Geochronological framework

Our results indicate that the difference between the oldest and the youngest reported age from Patmos and Chiliomodi is 1.370 ± 0.063 Ma (excluding data KB11), so there was a brief volcanic period of ~ 1.4 Ma with at least three distinct intervals of activity: the oldest volcanic activity yielded phonolites at ~ 6.5 Ma, followed by the rhyolitic and trachytic volcanism on Patmos island around ~ 6.0 Ma, and volcanic activity on Chiliomodi island around ~ 5.8 Ma. The accuracy, sample complexity and number of the individual dates does not allow further distinction of intervals, although there might be more.

In contrast with Fytikas et al. (1976) and Wyers (1987a), we have not found evidence for > 6.0 Ma ages in the trachytic rocks. The first K/Ar ages for Patmos were reported

by Fytikas et al. (1976). They obtained 4.38 ± 0.15 Ma for a whole rock sample of an alkali basalt lava flow of Chiliomodi (PAT-12), 7.03 ± 0.025 Ma for biotite and groundmass of a trachyte lava dome of Lefki Bay (PAT-34), and 7.20 ± 0.025 Ma for biotite of a trachytic intrusive facies of Prasso. (PAT-28). Wyers (1987a) dated five whole rock (WR) samples (rhyolite, phonolites, ne-trachybasalt, hy-trachybasalt and hy-trachyandesite) with the K/Ar method and three WR samples (trachyte and young and older ne-trachybasalt) with the $^{40}Ar/^{39}Ar$ method. Decay constants and standard conventions were not reported, and thus direct comparison is difficult, leading to an additional uncertainty between the older and the new results of > 1 %. Further, the whole rock approach has shown difficulties, and modern $^{40}Ar/^{39}Ar$ geochronology dates either groundmass (without phenocrysts) or the K-bearing phenocrysts in volcanic rocks. Moreover, the youngest samples (4.49–4.64 Ma) of Wyers (1987a) have very low radiogenic $^{40}Ar^*$ yields (< 32 %) and suggest alteration and/or Ar loss similar to biotite sample P11. Due to these uncertainties, these previously published ages are not included in the present discussion.

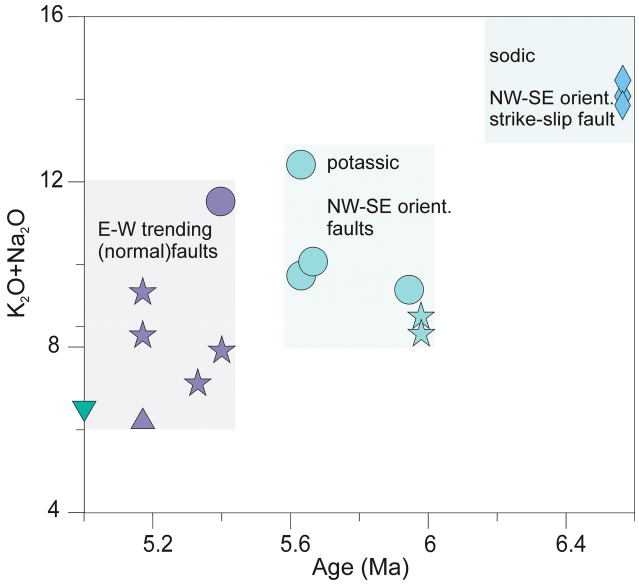

Figure 4. $K_2O + Na_2O$ versus age (in Ma). This diagram shows the volcanic rocks of Chiliomodi (purple field), the volcanic rocks of Patmos (turquoise) and the phonolites of Patmos (blue).

4.3 Alkalinity of the volcanism

The ratio of K_2O/Na_2O demonstrates the chronological evolution from sodic for the oldest rocks of Patmos (phonolites) to potassic (trachytes Patmos island) and again to (almost) sodic nature (Chiliomodi rhyolites; Fig. 4). The sodic character of the phonolites is one characteristic of a possible asthenospheric influence. Although high $K_2O + Na_2O$ volcanics are the norm, the Chiliomodi rhyolite (P1) also contains andesitic enclaves that represent quenched magma compositions with a lower $K_2O + Na_2O$ content, comparable to the trachybasalt of Chiliomodi and the volcanics from Nisyros and Kolumbo (Fig. 2b). The volcanic rocks of Chiliomodi island have similar Na_2O contents to the volcanics of South Aegean active Volcanic Arc (SAVA) and Kula, which are common geochemical proxies used in the area (Fig. 2b). The trend in the youngest volcanics of our study (Chiliomodi trachybasalt, trachyte, rhyolites and enclave) is in agreement with the general more sodic trend observed towards the Quaternary, which is also manifested in the relatively sodic nature of the Kula basalts.

4.4 Tectonic constraints for Patmos

Stratigraphy on Patmos started with marble basement rocks and deposition of epiclastics (Galeos, 1993). On the Diakofti Cape in the south of Patmos, epiclastics occur as almost vertical banks intercalated with NW–SE-trending rhyolitic–trachytic dykes and basic dykes. If there is no unconformity at the base of the epiclastics and if we assume that the other occurrences of epiclastics on Patmos are not tilted (Galeos, 1993), then the vertical beds within the epiclastics may be an effect of transfer faulting (Fig. 1b; Uzel et al., 2013, 2020).

Tectonic setting and magmatic activity are often argued to be closely related. Large-scale and regional plate tectonic settings govern the formation of magma, and local tectonic stress fields dictate whether magma can reach the surface. The dated rocks of this study show correlations with different tectonic features. (1)The two localities where phonolites, the oldest dated rocks of this study, are found on Patmos lie on a NW–SE-orientated strike-slip fault (for fault data, see Ring et al., 2017; dashed lines in Fig. 1b), i.e. a conjugate fault to the NE–SW-orientated large-scale transfer faults (such as the İzmir-Balıkesir Transfer Zone, İBTZ, and the Mid-Cycladic Lineament, MCL). If the İBTZ (or West Anatolian Shear Zone; Gessner et al., 2013) is marking the western end of the slap gap between the Aegean and Cyprus slab, a crustal-scale conjugate fault on Patmos could be an expression of the slab edge and local asthenospheric upwelling could be easily explained, similar to western Anatolia (Uzel et al., 2020). (2) The volcanic activity continued between 6.0 and 5.6 Ma with the eruption of rhyolites and trachytes on Patmos. The localities are situated close to NW–SE-orientated faults. A short-term inversion along the transfer zone is possible. At the same time the pulse of asthenospheric upwelling faded. (3) At 5.4 Ma we suggest another tectonic change to E–W-trending (normal) faults, which facilitated the eruption of the Chiliomodi volcanics including the young basalts. We hypothesize that high-angle normal faulting became dominant in the horst–graben development phase of post-Late Miocene extension. Interestingly, a transition from submarine to terrestrial extrusion is described in the literature for the basalts (Galeos, 1993), which could mean either that there was a short period of contraction (Kocygit et al., 1999) and uplift

within the main stress field of extension or that this transition describes a sea level drop.

5 Conclusion

In this study we presented a revised tectonic interpretation based on new high-resolution geochronology for Patmos. We provide 12 new sanidine and 2 new biotite $^{40}Ar/^{39}Ar$ ages on nine different samples. With this approach we analyse biotite and sanidine on the same sample and multiple sanidine sample splits with either different grain sizes or different magnetic behaviour. This allows us to present high-quality results with high internal reproducibility within each sample fraction, and this supports the reliability of our age results for resolving the characteristics of the < 1.5 Myr interval of volcanism on Patmos.

Our new age data for Patmos and the nearby small island of Chiliomodi indicate a brief volcanic period with three distinct volcanic intervals. Summarizing the results, we draw the following conclusions. (1) Magmatism with an asthenospheric to intraplate signature on Patmos started at 6.5 Ma with the eruption of sodic phonolites. A crustal-scale NW–SE-orientated strike-slip fault in combination with a gap between subduction slabs below facilitated the rise of the asthenospheric mantle. (2) The next phase of magmatism from 6.0 to 5.6 Ma produced rhyolites and trachytes that have a more potassic nature. This could mean that the influx of asthenosphere mantle diminished and the influence of subcontinental lithospheric mantle increased. This can be linked to a short-term inversion along the transfer zone or to the transition from strike-slip to normal faulting that resulted from this process. (3) Along with another tectonic change to E–W-orientated faults, trachytic and rhyolitic volcanism on Chiliomodi commenced at 5.4 Ma and lasted until 5.2 Ma.

Code availability. The following software code was used https://doi.org/10.1016/S0098-3004(01)00095-4 (Koppers, 2002).

Data availability. The dataset is found in the Supplement to this paper.

Supplement. The supplement related to this article is available online at: https://doi.org/10.5194/gchron-5-391-2023-supplement.

Author contributions. KMB, JRW and KFK were involved in the main conceptualization. KMB carried out the geochronological experiments and data reduction, with support from KFK and JRW. PZV did XRF experiments, and BU provided tectonic input. KMB prepared the manuscript and visualization with reviews and editing from JRW, KMB and BU. Acquisition of the financial support for the project was done by JRW, PZV and KFK.

Competing interests. The contact author has declared that none of the authors has any competing interests.

Disclaimer. Publisher's note: Copernicus Publications remains neutral with regard to jurisdictional claims in published maps and institutional affiliations.

Acknowledgements. Permission for fieldwork and sampling was kindly provided by the Greek Institute of Geology and Mineral Exploration. Athanasios Godelitsas and Gregor Hofer are thanked for great assistance in the field, and Roel van Elsas and Marjolein Daeter are greatly acknowledged for analytical assistance. Further, Naomi Lamers is thanked for the XRF analysis and thin-section photographs.

Financial support. This research has been supported by the Netherlands Research Centre for Integrated Solid Earth Sciences (grant no. 834.09.004).

Review statement. This paper was edited by Klaus Mezger and reviewed by Uwe Ring and one anonymous referee.

References

Agostini, S., Doglioni, C., Innocenti, F., Manetti, P., and Tonarini, S.: On the geodynamics of the Aegean rift, Tectonophysics, 488, 7–21, 2010.

Akal, C., Helvacı, C., Prelević, D., and van den Bogaard, P.: High-K volcanism in the Afyon region, western Turkey: from Si-oversaturated to Si-undersaturated volcanism, Int. J. Earth Sci., 102, 435–453, 2013.

Akay, E. and Erdoğan, B.: Evolution of Neogene calc-alkaline to alkaline volcanism in the Aliağa-Foça region (Western Anatolia, Turkey), J. Asian Earth Sci., 24, 367–387, 2004.

Alıcı, P., Temel, A., and Gourgaud, A.: Pb–Nd–Sr isotope and trace element geochemistry of Quaternary extension-related alkaline volcanism: a case study of Kula region (western Anatolia, Turkey), J. Volcanol. Geoth. Res., 115, 487–510, 2002.

Altunkaynak, S., Rogers, N. W., and Kelley, S. P.: Causes and effects of geochemical variations in late Cenozoic volcanism of the Foca volcanic centre, NW Anatolia, Turkey, Int. Geol. Rev., 52, 579–607, 2010.

Anderson, A. T., Davis, A. M., and Lu, F.: Evolution of Bishop Tuff rhyolitic magma based on melt and magnetite inclusions and zoned phenocrysts, J. Petrol., 41, 449–473, 2000.

Armijo, R., Meyer, B., Hubert, A., and Barka, A.: Westward propagation of the North Anatolian fault into the northern Aegean: Timing and kinematics, Geology, 27, 267–270, 1999.

Armijo, R., Meyer, B., Navarro, S., King, G., and Barka, A.: Asymmetric slip partitioning in the Sea of Marmara pull-apart: A clue to propagation processes of the North Anatolian fault?, Terra Nova, 14, 80–86, 2002.

Biedermann, A. R., Pettke, T., Angel, R. J., and Hirt, A. M.: Anisotropy of magnetic susceptibility in alkali feldspar and pla-

gioclase, Geophysical Supplements to the Monthly Notices of the Royal Astronomical Society, 205, 479–489, 2016.

Biryol, C. B., Beck, S. L., Zandt, G., and Özacar, A. A.: Segmented African lithosphere beneath the Anatolian region inferred from teleseismic P-wave tomography, Geophys. J. Int., 184, 1037–1057, 2011.

Bozkurt, E. and Mittwede, S. K.: Introduction: Evolution of continental extensional tectonics of western Turkey, Geodin. Acta, 18, 153–165, 2005.

Çoban, H. and Flower, M. F.: Mineral phase compositions in silica-undersaturated "leucite" lamproites from the Bucak area, Isparta, SW Turkey, Lithos, 89, 275–299, 2006.

Duermeijer, C. E., Krijgsman, W., Langereis, C. G., and Ten Veen, J. H.: Post-early Messinian counterclockwise rotations on Crete: implications for Late Miocene to Recent kinematics of the southern Hellenic arc, Tectonophysics, 298, 177–189, 1998.

Elitok, Ö.: Geology and petrology of the potassic and ultrapotassic rocks from the northern part of Senirkent (Isparta-SW Turkey): evidence of magma–carbonate wall-rock interactions, Arab. J. Geosci., 12, 289, https://doi.org/10.1007/s12517-019-4453-6, 2019.

Ersoy, E. Y. and Palmer, M. R.: Eocene-Quaternary magmatic activity in the Aegean: Implications for mantle metasomatism and magma genesis in an evolving orogeny, Lithos, 180, 5–24, 2013.

Finch, A. A. and Klein, J.: The causes and petrological significance of cathodoluminescence emissions from alkali feldspars, Contrib. Mineral. Petrol., 135, 234–243, 1999.

Fytikas, M., Giuliani, O., Innocenti, F., Marinelli, G. T., and Mazzuoli, R.: Geochronological data on recent magmatism of the Aegean Sea, Tectonophysics, 31, T29–T34, 1976.

Galeos, A.: Geological map of Greece-Patmos island sheet 1.50.000, IGME, Athens, Greece, https://shop.geospatial.com/product/CAFVME9BP47C45EXS3333W5TY5/255-Patmos-Sheet-Greece-1-to-50000-Scale-Geological-Maps (last access: 7 October 2023), 1993.

Gessner, K., Gallardo, L. A., Markwitz, V., Ring, U., and Thomson, S. N.: What caused the denudation of the Menderes Massif: Review of crustal evolution, lithosphere structure, and dynamic topography in southwest Turkey, Gondwana Res., 24, 243–274, 2013.

Govers, R. and Fichtner, A.: Signature of slab fragmentation beneath Anatolia from full-waveform tomography, Earth Planet. Sc. Lett., 450, 10–19, 2016.

Hess, J. C., Lippolt, H. J., and Wirth, R.: Interpretation of $^{40}Ar^{39}Ar$ biotites: Evidence from hydrothermal degassing experiments and TEM studies, Chem. Geol., 66, 137–149, 1987.

Hora, J. M., Singer, B. S., Jicha, B. R., Beard, B. L., Johnson, C. M., de Silva, S., and Salisbury, M.: Volcanic biotite-sanidine $^{40}Ar/^{39}Ar$ age discordances reflect Ar partitioning and pre-eruption closure in biotite: Geology, 38, 923–926, 2010.

Horvath, F. and Berckhemer, H.: Mediterranean backarc basins, Alpine-Mediterranean Geodynamics, 7, 141–173, 1982.

Hounslow, M. W. and Morton, A. C.: Evaluation of sediment provenance using magnetic mineral inclusions in clastic silicates: comparison with heavy mineral analysis, Sediment. Geol., 171, 13–36, 2004.

Jacobshagen, V.: Orogenic evolution of the Hellenides: new aspects, in: Active Continental Margins – Present and Past, edited by: Giese, P. and Behrman, J., Springer, Berlin, Heidelberg, Germany, 249–256, https://doi.org/10.1007/978-3-662-38521-0, 1994.

Jacobshagen, V., Duerr, J., Kockel, F., Kowalczyk, G., and Berckhemer, H.: Structure and geodynamic evolution of the Aegean region, in: Alps, Apennines, Hellenides, Volume report 38, edited by: Cloos, H., Roeder, D., and Schmidt, K., Stuttgart, E. Schweizerbart'sche, 537–564, 1978.

Jolivet, L. and Brun, J. P.: Cenozoic geodynamic evolution of the Aegean, Int. J. Earth Sci., 99, 109–138, 2010.

Jolivet, L., Arbaret, L., Le Pourhiet, L., Cheval-Garabédian, F., Roche, V., Rabillard, A., and Labrousse, L.: Interactions of plutons and detachments: a comparison of Aegean and Tyrrhenian granitoids, Solid Earth, 12, 1357–1388, https://doi.org/10.5194/se-12-1357-2021, 2021.

Kissel, C. and Laj, C.: The Tertiary geodynamical evolution of the Aegean arc: a paleomagnetic reconstruction, Tectonophysics, 146, 183–201, 1988.

Klaver, M., Djuly, T., de Graaf, S., Sakes, A., Wijbrans, J., Davies, G., and Vroon, P.: Temporal and spatial variations in provenance of Eastern Mediterranean Sea sediments: Implications for Aegean and Aeolian arc volcanism, Geochim. Cosmochim. Ac., 153, 149–168, 2015.

Klaver, M., Carey, S., Nomikou, P., Smet, I., Godelitsas, A., and Vroon, P.: A distinct source and differentiation history for Kolumbo submarine volcano, Santorini volcanic field, Aegean arc, Geochem. Geophy. Geosys., 17, 3254–3273, 2016.

Koçyigit, A., Yusufoglu, H., and Bozkurt, E.: Discussion on evidence from the Gediz Graben for episodic two-stage extension in western Turkey, J. Geol. Soc. Lond., 156, 1240–1242, 1999.

Koppers, A. A.: ArArCALC – software for $^{40}Ar/^{39}Ar$ age calculations, Comput. Geosci., 28, 605–619, 2002.

Kuiper, K. F., Hilgen, F. J., Steenbrink, J., and Wijbrans, J. R.: $^{40}Ar/^{39}Ar$ ages of tephras intercalated in astronomically tuned Neogene sedimentary sequences in the eastern Mediterranean, Earth Planet. Sc. Lett., 222, 583–597, 2004.

Le Bas, M., Le Maitre, R., Streckeisen, A., and Zanettin, B.: A chemical classification of volcanic rocks based on the total alkali-silica diagram, J. Petrol., 27, 745–750, 1986.

Le Pichon, X. and Angelier, J.: The Aegean Sea, Philos. T. Roy. Soc. A, 300, 357–372, 1981.

Lee, J.-Y., Marti, K., Severinghaus, J. P., Kawamura, K., Yoo, H.-S., Lee, J. B., and Kim, J. S.: A redetermination of the isotopic abundances of atmospheric Ar, Geochim. Cosmochim. Ac., 70, 4507–4512, 2006.

Lips, A. L., Cassard, D., Sözbilir, H., Yilmaz, H., and Wijbrans, J. R.: Multistage exhumation of the Menderes massif, western Anatolia (Turkey), Int. J. Earth Sci., 89, 781–792, 2001.

Lykousis, V., Anagnostou, C., Pavlakis, P., Rousakis, G., and Alexandri, M.: Quaternary sedimentary history and neotectonic evolution of the eastern part of Central Aegean Sea, Greece, Mar. Geol., 128, 59–71, 1995.

McKenzie, D.: Active tectonics of the Alpine–Himalayan belt: the Aegean Sea and surrounding regions, Geophys. J. Int., 55, 217–254, 1978.

Palmer, M., Ersoy, E. Y., Akal, C., Uysal, İ., Genç, Ş., Banks, L., Cooper, M., Milton, J., and Zhao, K.: A short, sharp pulse of potassium-rich volcanism during continental collision and subduction: Geology, 47, 1079–1082, 2019.

Pe-Piper, G. and Piper, D. J.: Neogene backarc volcanism of the Aegean: new insights into the relationship between magmatism and tectonics, 2007.

Pe-Piper, G., Zhang, Y., Piper, D. J., and Prelević, D.: Relationship of Mediterranean type lamproites to large shoshonite volcanoes, Miocene of Lesbos, NE Aegean Sea, Lithos, 184, 281–299, 2014.

Prelević, D., Akal, C. Ü. N. E. Y. T., Foley, S. F., Romer, R. L., Stracke, A., and Van Den Bogaard, P.: Ultrapotassic mafic rocks as geochemical proxies for post-collisional dynamics of orogenic lithospheric mantle: the case of southwestern Anatolia, Turkey, J. Petrol., 53, 1019–1055, 2012.

Prelević, D., Akal, C., Romer, R. L., Mertz-Kraus, R., and Helvacı, C.: Magmatic response to slab tearing: constraints from the Afyon Alkaline Volcanic Complex, Western Turkey, J. Petrol., 56, 527–62, 2015.

Ring, U., Laws, S., and Bernet, M.: Structural analysis of a complex nappe sequence and late-orogenic basins from the Aegean Island of Samos, Greece, J. Struct. Geol., 21, 1575–1601, 1999.

Ring, U., Gessner, K., and Thomson, S.: Variations in fault-slip data and cooling history reveal corridor of heterogeneous backarc extension in the eastern Aegean Sea region, Tectonophysics, 700, 108–130, 2017.

Robert, U.: Les roches volcaniques de l'île de Patmos (Dodecanese Grece), These 3e cycle, Univ. Paris, 159 pp., 1973.

Roche, V., Conand, C., Jolivet, L., and Augier, R.: Tectonic evolution of Leros (Dodecanese, Greece) and correlations between the Aegean Domain and the Menderes Massif, J. Geol. Soc., 175, 836–849, 2018.

Roche, V., Jolivet, L., Papanikolaou, D., Bozkurt, E., Menant, A., and Rimmelé, G.: Slab fragmentation beneath the Aegean/Anatolia transition zone: Insights from the tectonic and metamorphic evolution of the Eastern Aegean region, Tectonophysics, 754, 101–129, 2019.

Smith, M. E., Singer, B. S., Carroll, A. R., and Fournelle, J. H.: Precise dating of biotite in distal volcanic ash: Isolating subtle alteration using $^{40}Ar/^{39}Ar$ laser incremental heating and electron microprobe techniques, Am. Mineral., 93, 784–795, 2008.

Soder, C., Altherr, R., and Romer, R. L.: Mantle metasomatism at the edge of a retreating subduction zone: Late Neogene lamprophyres from the Island of Kos, Greece, J. Petrol., 57, 1705–1728, 2016.

Uzel, B., Sözbilir, H., Özkaymak, Ç., Kaymakcı, N., and Langereis, C. G.: Structural evidence for strike-slip deformation in the İzmir–Balıkesir transfer zone and consequences for late Cenozoic evolution of western Anatolia (Turkey), J. Geodyn., 65, 94–116, 2013.

Uzel, B., Langereis, C. G., Kaymakci, N., Sözbilir, H., Özkaymak, Ç., and Özkaptan, M.: Paleomagnetic evidence for an inverse rotation history of Western Anatolia during the exhumation of Menderes core complex, Earth Planet. Sc. Lett., 414, 108–125, 2015.

Uzel, B., Kuiper, K., Sözbilir, H., Kaymakci, N., Langereis, C. G., and Boehm, K.: Miocene geochronology and stratigraphy of western Anatolia: Insights from new Ar/Ar dataset, Lithos, 352, 105305, https://doi.org/10.1016/j.lithos.2019.105305, 2020.

Van Hinsbergen, D. J. J., and Schmid, S. M.: Map view restoration of Aegean-West Anatolian accretion and extension since the Eocene, Tectonics, 31, https://doi.org/10.1029/2012TC003132, 2012.

Wijbrans, J. R. and McDougall, I.: Metamorphic evolution of the Attic Cycladic Metamorphic Belt on Naxos (Cyclades, Greece) utilizing $^{40}Ar/^{39}Ar$ age spectrum measurements, J. Metamorph. Geol., 6, 571–594, 1988.

Wyers, G. P.: Petrogenesis of calc-alkaline and alkaline magmas from the southern and eastern Aegean Sea, Greece, The Ohio State University, 1987a.

Wyers, G. P.: Geochemistry of a transitional ne-trachybasalt–Q-trachyte lava series from Patmos (Dodecanesos), Greece: further evidence for fractionation, mixing and assimilation, Contrib. Mineral. Petr., 97, 279–291, 1987b.

Wyers, G. P. and Barton, M.: Petrology and evolution of transitional alkaline–sub alkaline lavas from Patmos, Dodecanesos, Greece: evidence for fractional crystallization, magma mixing and assimilation, Contrib. Mineral. Petr., 93, 297–311, 1986.